Reconstructing the Ocean's Interior from Surface Data

Reconstructing the Ocean's Interior from Surface Data

JINBO WANG

Woods Hole Oceanographic Institution, Woods Hole, Massachusetts

GLENN R. FLIERL

Massachusetts Institute of Technology, Cambridge, Massachusetts

JOSEPH H. LACASCE

Department of Geosciences, University of Oslo, Oslo, Norway

JULIE L. MCCLEAN

Scripps Institution of Oceanography, University of California, San Diego, La Jolla, California

AMALA MAHADEVAN

Woods Hole Oceanographic Institution, Woods Hole, Massachusetts

(Manuscript received 14 October 2012, in final form 1 March 2013)

ABSTRACT

A new method is proposed for extrapolating subsurface velocity and density fields from sea surface density and sea surface height (SSH). In this, the surface density is linked to the subsurface fields via the surface quasigeostrophic (SQG) formalism, as proposed in several recent papers. The subsurface field is augmented by the addition of the barotropic and first baroclinic modes, whose amplitudes are determined by matching to the sea surface height (pressure), after subtracting the SQG contribution. An additional constraint is that the bottom pressure anomaly vanishes. The method is tested for three regions in the North Atlantic using data from a high-resolution numerical simulation. The decomposition yields strikingly realistic subsurface fields. It is particularly successful in energetic regions like the Gulf Stream extension and at high latitudes where the mixed layer is deep, but it also works in less energetic eastern subtropics. The demonstration highlights the possibility of reconstructing three-dimensional oceanic flows using a combination of satellite fields, for example, sea surface temperature (SST) and SSH, and sparse (or climatological) estimates of the regional depth-resolved density. The method could be further elaborated to integrate additional subsurface information, such as mooring measurements.

1. Introduction

Over the past two decades, satellites have mapped the ocean surface with global coverage at fairly high spatial and temporal resolution, sufficient for detecting many mesoscale features in the ocean. However, satellites only reveal the surface fields. To fully exploit this information, we require a method to project those fields into the ocean interior. How to do this has been an ongoing discussion in recent years.

Early studies suggested that the satellite altimetric signal mainly reflects the interior barotropic and first baroclinic modes. For instance, Stammer (1997) analyzed the frequency–wavenumber spectra for the first three years of data from the Ocean Topography Experiment (TOPEX)/Poseidon altimeter and found that the eddy scales are proportional to the Rossby deformation radius of the first baroclinic mode, suggesting in turn that surface height deviations are linked to those of the main thermocline. Wunsch (1997) examined the vertical partition of horizontal kinetic energy using data

Corresponding author address: Jinbo Wang, Woods Hole Oceanographic Institution, MS #29, Woods Hole, MA 02543.
E-mail: jinbow@alum.mit.edu

DOI: 10.1175/JPO-D-12-0204.1

from a large number of globally distributed current meter records. The barotropic and the first baroclinic modes accounted for the largest share of the depth-averaged energy, while the first baroclinic mode dominated surface variability. The dominance of these two modes is consistent with the theory of Fu and Flierl (1980), as with subsequent observational (Chelton et al. 2011) and numerical studies (Smith and Vallis 2001).

The baroclinic modes are orthogonal and form a complete basis. In most studies, the modes are obtained by demanding that the buoyancy anomaly (and consequently, the vertical pressure gradient) vanishes at the surface and bottom (e.g., Kundu and Allen 1975). Thus, the modes do not account for buoyancy anomalies at the surface, induced, for example, by the stirring of large-scale temperature gradients. Recent studies suggest that sea surface buoyancy anomalies can in fact be important and affect the vertical partition of the horizontal kinetic energy (Lapeyre 2009; Ferrari and Wunsch 2010). But the relative importance of such anomalies and the traditional baroclinic modes remains to be determined.

Generally, one can think of the interior flow as stemming from two sources. One is the potential vorticity (PV) in the interior of the fluid. If one knows the PV, one can invert the PV equation (exploiting the quasigeostrophic approximation) to obtain the streamfunction, given the background stratification (Hoskins 1975; Pedlosky 1987). A second source is buoyancy/density anomalies on the boundaries, which act as PV sheets (Bretherton 1966) and also contribute to the interior flow (Eady 1949; Charney 1971).

The flow induced by density anomalies can be obtained via the surface quasigeostrophic (SQG) construct. In this, the interior PV is assumed constant (typically zero). The approach has been used fruitfully in the troposphere, where the interior PV is typically weak (Blumen 1978; Hoskins 1975; Tulloch and Smith 2006, 2009). The Brunt–Väisälä frequency in the troposphere is, moreover, nearly constant, which facilitates analytical solutions. SQG solutions have also been applied to oceanic flows (LaCasce and Mahadevan 2006; Lapeyre and Klein 2006; Isern-Fontanet et al. 2008). A common feature among these studies is that the SQG solution tends to underpredict the subsurface flow, given realistic values of N^2. A possible reason is that N^2 is not constant in the ocean interior. In fact, using a more realistic (exponential) stratification weakens the subsurface response even further (LaCasce 2012).

Another explanation is that the subsurface PV is not zero. However, the difficulty is that the subsurface PV is not observable from space and we do not know its structure or amplitude. LaCasce and Mahadevan (2006) proposed that the PV could be derived from the surface density using an empirical relationship, which they diagnosed from in situ data. This succeeded in increasing the subsurface response. However, the structure of the PV (an exponential function) was chosen largely as a matter of convenience.

An alternate approach was suggested by Lapeyre and Klein (2006). The authors suggested that surface buoyancy anomalies should be anticorrelated with the interior PV because both fields, forced by baroclinic instability of the large-scale flow, are stirred by the same eddy field. The assumed anticorrelation leads to a simplified relationship between sea surface height (SSH) and the surface buoyancy anomaly, that is, $\eta \sim b^s$ where η represents SSH and b^s the surface buoyancy (Isern-Fontanet et al. 2006, 2008; Klein et al. 2009). With this, one can obtain the subsurface flow using the SQG solution, suitably adjusted. The adjustment is accomplished by modifying N^2 (which is assumed to be constant).

Both methods implicitly assume that the surface density and interior PV are correlated. In fact, the two fields are often quite different. Were they perfectly correlated (or anticorrelated), the sea surface height would resemble the surface density. But satellite SSH and SST anomalies, shown in one instance for a region of the northeast Atlantic in Fig. 1, are not always coincident. (In using SST, we assume that temperature dominates the surface density variations for lack of an equivalent surface salinity field.) While there are regions where SST and SSH anomalies are correlated, there are others where they are not. Using a modified form of SQG would not work in these latter regions.

There are at least two explanations for why surface density could differ from surface pressure. One stems from the surface mixed layer. Surface heating/cooling can modify the surface signature of near-surface density anomalies, changing possibly both their strength and lateral structure (LaCasce and Mahadevan 2006). Isern-Fontanet et al. (2008) found that their SQG-based reconstruction of the subsurface vorticity in the North Atlantic was most successful where the mixed layer was deep; where it was shallow, surface forcing had evidently altered the surface expression.

Second, interior PV can affect surface pressure without affecting the surface density. An example is the Phillips (1954) model of baroclinic instability. This has nonzero PV in the interior (as a result of the mean baroclinic shear), but zero buoyancy anomaly on the top and bottom boundaries. Instability in the model produces eddies with nonvanishing pressure on the boundaries, but no density anomaly.

Recently Smith and Vanneste (2013) propose a new set of basis functions to replace the traditional baroclinic modes that simultaneously match the

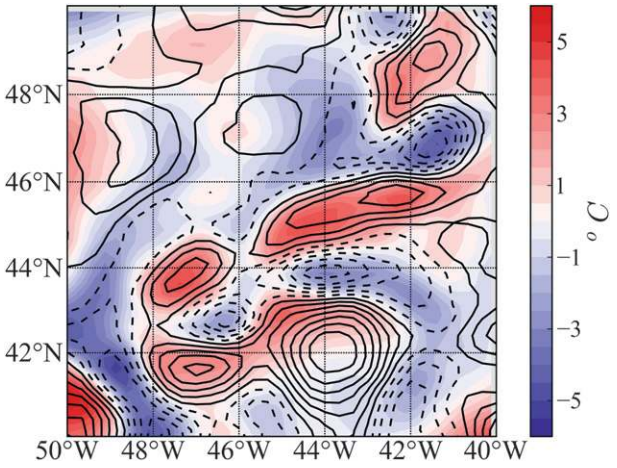

FIG. 1. Satellite-derived SST anomaly (color) superimposed with the SSH anomaly (contours) over the northeast Atlantic Ocean on 5 Jan 2005. SST data are from Reynolds et al. (2007). SSH is from Archiving, Validation, and Interpretation of Satellite Oceanographic data (AVISO). The anomaly (eddy) fields are obtained by subtracting the respective low-pass-filtered fields from the SST and SSH data.

density and pressure at the surface and bottom. These modes can be used as an alternative approach for the reconstruction. However, as the problem is nonunique, additional assumptions must be invoked for the modes selection. The method is distinct from the one proposed here, which has the additional benefit of simplicity.

Indeed, as the quasigeostrophic PV equation is linear, it admits a superposition of solutions. So one can isolate the SQG and interior solutions (Blumen 1978; Lapeyre and Klein 2006; Ferrari and Wunsch 2010), where the latter, constructed ideally from surface data, would account for the interior PV. This is the basis of the present approach. The key point is the recognition that both SQG and interior fields contribute to the surface and bottom pressure.

In what follows (section 2), we lay out a quasigeostrophic (QG) framework that combines the SQG and interior solutions. The latter are projected onto a truncated set of vertical normal modes. We term our approach the interior plus surface QG (isQG) method. Importantly, the isQG method is quasigeostrophic and as such applies to situations and scales (10–500 km) where the QG approximation is valid. It reconciles the fundamental dichotomy between the two approaches (SQG and normal modes) that have individually gained importance for describing the vertical structure of the ocean interior. In section 3, we test the proposed isQG approach by using fields from the Parallel Ocean Program (POP) three-dimensional primitive equation (PE) model solution of the North Atlantic. The isQG method is used to diagnose the interior fields from the spatially averaged vertical buoyancy gradient (N^2) profile, sea surface density, and sea surface height fields at an instance in time within three chosen subdomains of the PE model domain. The diagnosed interior solution is compared to the full PE solution and the results are discussed for each of the regions. Finally, in section 4, we provide a discussion of the results and caveats of the method.

2. The interior plus surface QG method

Consider a flow in quasigeostrophic balance. The QG approximation is relatively accurate for scales from 10 to 500 km (Charney and Flierl 1981) and greatly simplifies the equations of motion. The dynamics are determined by a scalar quantity, the potential vorticity (QGPV), which is advected by the geostrophic flow. The geostrophic flow in turn is determined by inverting the PV (Hoskins et al. 1985). The two are related by

$$\mathcal{L}\Psi + f_0 + \beta y = Q,$$
$$\mathcal{L} = \left(\frac{\partial^2}{\partial x^2} + \frac{\partial^2}{\partial y^2} + \frac{\partial}{\partial z}\frac{f_0^2}{N^2}\frac{\partial}{\partial z}\right), \quad \text{and} \quad -H < z < 0, \quad (1)$$

where f_0 is the mean Coriolis parameter in the region, β is the meridional gradient of the planetary vorticity, $N^2 = -(g/\rho)(\partial\rho/\partial z)$ is the Brunt–Väisälä frequency, $\Psi = p(\rho_0 f_0)^{-1}$ is the geostrophic streamfunction, and Q is the QGPV (Pedlosky 1987).

We partition the fields into the large-scale background flow and perturbation (eddy) components. The PV balance for the former is

$$\mathcal{L}\langle\Psi\rangle + f_0 + \beta y = \langle Q\rangle, \quad (2)$$

where $\langle\cdot\rangle$ indicates low-pass filtering, whose specific form is defined in section 3. The PV equation for the eddy field, $\psi = \Psi - \langle\Psi\rangle$, is then a simple elliptic equation, given by

$$\mathcal{L}\psi = q(x, y, z, t). \quad (3)$$

Given q, one can obtain the streamfunction.

This in turn requires boundary conditions, in particular on the upper and lower horizontal surfaces. The conditions, which derive from the QG density equation, are given by

$$\frac{\partial}{\partial z}\psi(\mathbf{x}, 0, t) = f_0^{-1} b(\mathbf{x}, 0, t) \quad \text{and} \quad (4)$$

$$\frac{\partial}{\partial z}\psi(\mathbf{x}, -H, t) = f_0^{-1} b(\mathbf{x}, -H, t), \quad (5)$$

where $\mathbf{x} = (x, y)$, and $b = -g\rho/\rho_0$ is the buoyancy. Thus, with appropriate lateral boundary conditions (usually taken as periodic in the horizontal for a subdomain in the open ocean), the entire flow field can be deduced from the interior PV and the buoyancy on the upper and lower bounding surfaces.

As the operator $\mathcal{L}$ is linear, we can further decompose ψ into interior modes and surface (SQG) solutions (Charney 1971; Hoskins 1975; Ferrari and Wunsch 2010). The interior modes derive from the interior PV q^i, while the surface solutions derive from buoyancy anomalies on the boundaries. Specifically

$$\psi^t = \psi^i + \psi^s, \tag{6}$$

$$\mathcal{L}\psi^s = 0,$$

$$\frac{\partial}{\partial z}\psi^s(\mathbf{x}, z, t) = b(\mathbf{x}, z, t)/f_0 \quad \text{at} \quad z = 0, -H, \quad \text{and} \tag{7}$$

$$\mathcal{L}\psi^i = q^i, \quad \frac{\partial}{\partial z}\psi^i(\mathbf{x}, z, t) = 0 \quad \text{at} \quad z = 0, -H, \tag{8}$$

where ψ^t denotes the total streamfunction, ψ^s is the SQG solution, and ψ^i is the interior solution.

It is convenient to Fourier transform the variables in the horizontal, as follows:

$$\psi^i(x, y, z) = \sum_{k,l} \hat{\psi}^i(k, l, z) e^{ikx+ily}, \tag{9}$$

$$\psi^s(x, y, z) = \sum_{k,l} \hat{\psi}^s(k, l, z) e^{ikx+ily}, \tag{10}$$

$$q^i(x, y, z) = \sum_{k,l} \hat{q}^i(k, l, z) e^{ikx+ily}, \quad \text{and} \tag{11}$$

$$b(x, y, z) = \sum_{k,l} \hat{b}(k, l, z) e^{ikx+ily}. \tag{12}$$

Then (7) and (8) reduce to the ODEs:

$$\frac{\partial}{\partial z}\frac{f_0^2}{N^2}\frac{\partial}{\partial z}\hat{\psi}^s - \kappa^2\hat{\psi}^s = 0 \quad \text{with} \quad \frac{d\hat{\psi}^s}{dz} = \frac{1}{f_0}\hat{b}(k, l, z) \quad \text{at} \quad z = 0, -H \quad \text{and} \tag{13}$$

$$\frac{\partial}{\partial z}\frac{f_0^2}{N^2}\frac{\partial}{\partial z}\hat{\psi}^i - \kappa^2\hat{\psi}^i = \hat{q}^i \quad \text{with} \quad \frac{d\hat{\psi}^i}{dz} = 0 \quad \text{at} \quad z = 0, -H. \tag{14}$$

Because the SQG solutions that derive from (13) are linked solely to the surface, we assume that $\hat{b}(k, l, z) = 0$ at the lower boundary $z = -H$. Since we do not know the interior PV q^i, (14) is less tractable. The idea here is that we will project (14) onto baroclinic modes and then impose additional boundary conditions to deduce the gravest modes.

The baroclinic modes are the solutions to the Sturm–Liouville problem given by

$$\frac{\partial}{\partial z}\left(\frac{f_0^2}{N^2}\frac{\partial F_m}{\partial z}\right) = -R_m^{-2}F_m; \quad \frac{dF_m}{dz} = 0 \quad \text{at} \quad z = 0, -H. \tag{15}$$

Here, R_m is the Rossby deformation radius of the mth vertical mode, with $m = 0$ denoting the barotropic mode and $m > 0$ the baroclinic modes. A familiar example is $F_m = \cos(m\pi z/H)$, which is valid for $N^2 =$ constant (Pedlosky 1987).

The eigenfunctions F_m are orthonormal and comprise a complete set, so we can expand the interior ψ^i and PV vertical structure functions in terms of them, as

$$\hat{\psi}^i(k, l, z) = \sum_n A_n(k, l)F_n(z) \quad \text{and} \tag{16}$$

$$\hat{q}^i(k, l, z) = \sum_n B_n(k, l)F_n(z). \tag{17}$$

Substituting into (14) yields

$$\sum_n A_n \frac{\partial}{\partial z}\frac{f_0^2}{N^2}\frac{\partial}{\partial z}F_n - \kappa^2\sum_n A_n F_n = \sum_n B_n F_n. \tag{18}$$

With (15), this implies

$$B_n = -(R_n^{-2} + \kappa^2)A_n, \quad \text{where} \quad \kappa^2 = k^2 + l^2. \tag{19}$$

Thus, the coefficients for the PV (17) are related to the corresponding coefficients from the interior streamfunction (16). However, while $\hat{\psi}^s$ and F_n can be determined given the stratification $N^2(z)$, the coefficients A_n are unknown. But, we can determine some of them if we impose further constraints on the boundaries.

For instance, both the interior and surface portions of the streamfunction contribute to the sea surface height:

$$\psi^t(z = 0) = \psi^i(0) + \psi^s(0) = \frac{g}{f_0}\eta. \tag{20}$$

In terms of Fourier projections, this is

$$\hat{\psi}^s(k, l, 0) + \hat{\psi}^i(k, l, 0) = \frac{g}{f_0}\hat{\eta}(k, l), \tag{21}$$

where $\hat{\eta}$ is the amplitude of the projection of η at (k, l). Thus, given η, we can find $\hat{\psi}^i(k, l, 0)$ once $\hat{\psi}^s(k, l, 0)$ is calculated. If, in addition, we specify the bottom pressure anomaly, we obtain a second constraint. We will assume the bottom pressure anomaly vanishes, so that

$$\hat{\psi}^s(k,l,-H) + \hat{\psi}^i(k,l,-H) = 0. \quad (22)$$

With these two conditions and having determined F_m, one can determine the amplitudes of the first two modes A_0 and A_1 if we truncate the interior solution to two modes. Thus we obtain the reconstruction of the interior streamfunction onto the barotropic and first baroclinic modes. From (17) and (19), we can deduce the projection of the interior PV onto the same modes. Since oceanic variability is largely dominated by these gravest modes (Wunsch 1997; Scott and Furnival 2012), these solutions could potentially capture a significant portion of the signal. This appears to be the case, when evaluated against the solution of a three-dimensional PE numerical model.

The procedure is as follows. Given $N^2(z)$ at a particular location and $\hat{b}(k,l,z=0)$, we determine $\hat{\psi}^s(z)$ and $F_n(z)$; we do this numerically with details in the appendix. Then we impose the boundary conditions to determine the amplitudes, thus

$$\hat{\psi}^i(k,l,0) = A_0F_0(0) + A_1F_1(0) = \frac{g}{f_0}\hat{\eta} - \hat{\psi}^s(k,l,0) \quad \text{and} \quad (23)$$

$$\hat{\psi}^i(k,l,-H) = A_0F_0(-H) + A_1F_1(-H) = -\hat{\psi}^s(k,l,-H). \quad (24)$$

The system is easily solved, for example, via Cramer's rule.

The method outlined above has several limitations and assumptions. The method is quasigeostrophic and inverts for the eddy field associated with the anomalies over a region, assuming a regional average of $N^2(z)$ and a regional average of f. We assume that the horizontal variation in the stratification is sufficiently small not to impact the solution locally. The lateral boundary conditions are assumed to be periodic, which is reasonable for a subdomain in the open ocean away from continental boundaries. However, the horizontal periodicity is not a necessary condition if we directly solve the three-dimensional boundary value problem of (7) numerically in physical space instead of spectral space. The method does not account for bottom topography or surface forcing in any way, but assumes the surface buoyancy and height fields have assimilated these effects. Further, since we have only two boundary conditions, we are able to fit only the barotropic and first baroclinic mode. We assume the higher modes make a relatively small contribution. When implementing the method with satellite data, we would need to assume that the SST pattern reflects the surface buoyancy.

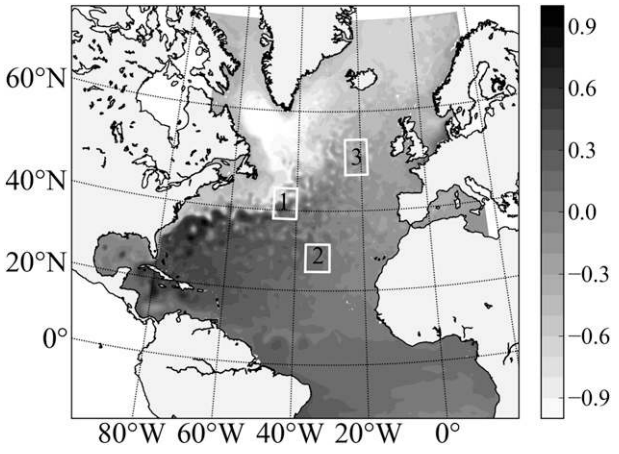

FIG. 2. A snapshot of the surface height (m) in the POP simulation. The three tested regions are marked by the three boxes.

In the following section, we use fields from a primitive equation (PE) model to demonstrate the method of diagnosing interior fields from surface data, which we then assess against the PE model solution itself.

3. Results of isQG inversion based on global circulation model fields

We assess the method on a GCM simulation of the North Atlantic (Fig. 2) using the Los Alamos National Laboratory (LANL) POP. The model was configured on a 1/10°, 40-level Mercator grid, the same as that used by Smith et al. (2000) and McClean et al. (2002). The model was spunup from rest for five years (1979–84) using forcing that was largely constructed from National Centers for Environmental Prediction (NCEP) fluxes (Doney et al. 2003). Surface momentum, heat, and salt fluxes were calculated using bulk formulae (Large et al. 1994) and a combination of daily NCEP analyses, monthly International Satellite Cloud Climatology Project (ISCCP) radiation data (Rossow and Schiffer 1991), and monthly Microwave Sounding Unit (MSU) (Spencer 1993) and the Xie and Arkin (1997) precipitation data. This spunup state was then used as the initial condition for the 1979–99 simulation; the 1995 model output was used for the analyses in this paper.

We choose three 7° × 7° subdomains (marked by the boxes in Fig. 2), representing three different dynamical regimes in which to test the isQG methodology. The first subdomain extends from 38° to 45°N and from 313° to 320°W, covering part of the Gulf Stream extension and its attendant eddy field. The second extends from 25° to 32°N and from 323° to 330°W, in the eastern part of the subtropical gyre. The third extends from 48° to 55°N and from 335° to 342°W, representing

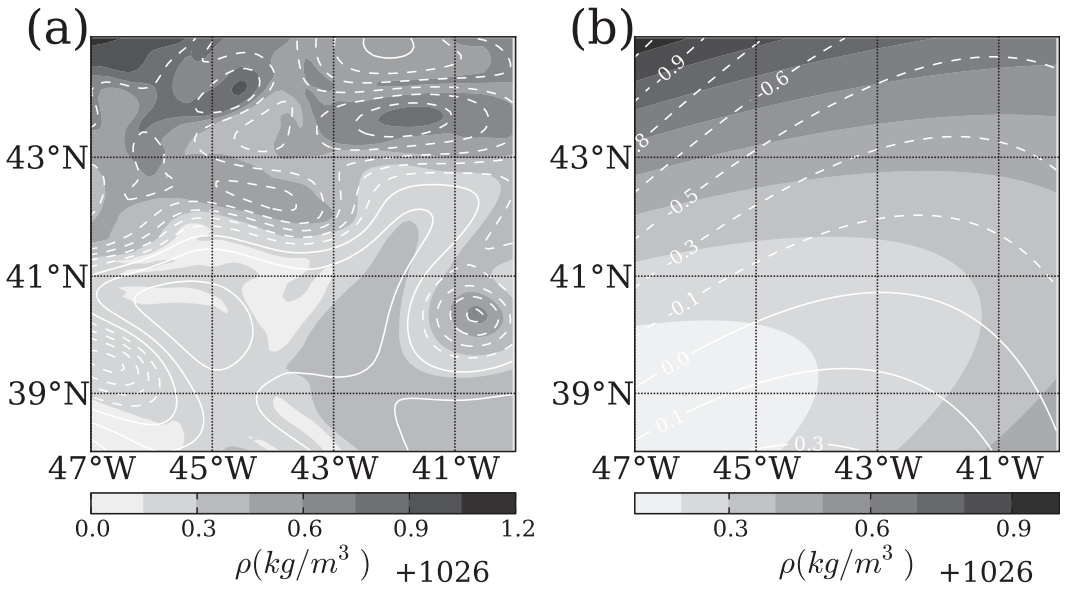

FIG. 3. (a) Time-averaged (23–29 January) sea surface density (shading) and SSH (contours) in the PE model. (b) The low-pass-filtered fields, denoted by $\langle\cdot\rangle$, obtained from a least squares fit of a quadratic surface to (a). The eddy fields are derived by subtracting (b) from (a).

high-latitude regions with weak stratification and deep mixed layers. Each of the regions is chosen away from continental boundaries, to avoid topographic effects.

The reconstruction requires three input fields: sea surface density (SSD), SSH, and the stratification $N^2(z)$. The 9-day-averaged sea surface density and SSH fields were preprocessed by subtracting their respective low-pass-filtered fields [denoted by $\langle\cdot\rangle$ in (2)], defined as a least squares fit of a the field to a quadratic surface $S(x, y)$,

$$S(x,y) = (C_0, C_1, C_2, C_3, C_4, C_5)(1,\, x,\, y,\, x^2,\, y^2,\, xy)^{\mathrm{T}}, \tag{25}$$

where x and y represent the zonal and meridional coordinates, respectively (both in metric units to account for the curvature of the earth surface). The eddy SSD field obtained by subtracting $\langle\rho\rangle$ from the SSD, gives the surface buoyancy anomaly, which is used to calculate the SQG solution ψ^s. The stratification used by the reconstruction is $N^2 = -(g/\rho_0)(\partial\overline{\rho}/\partial z)$, where ρ_0 is a reference potential density taken to be the volumetric mean, and $\overline{\rho}$ is the horizontal mean potential density in the corresponding $7^\circ \times 7^\circ$ subdomain.

The density anomaly and eddy velocity are calculated from reconstructed streamfunction as follows: $\rho = -(\rho_0 f/g)(\partial\psi/\partial z)$ and $\mathbf{u} = \mathbf{z} \times \nabla\psi$. These are evaluated against the density anomaly and eddy velocity in the PE model, which are obtained by subtracting the corresponding low-pass-filtered PE fields $\langle\cdot\rangle$ defined in (25). This low-pass filter functions similarly to the long-wave truncation used in (Isern-Fontanet et al. 2008) to remove the mean large-scale background flow. The low-pass-filtered field usually does not have a flat surface and varies in both zonal and meridional directions (Fig. 3b).

The three chosen regions of the PE model show different characteristics. The Gulf Stream extension is characterized by strong lateral density gradients and energetic eddies (Fig. 4a). The subdomain in the eastern subtropical gyre is characterized by weak eddies and a strong stratification at the base of the mixed layer (Figs. 4b,e). The high-latitude subdomain is characterized by a deep mixed layer and weak stratification (Figs. 4c,f), with relatively weak eddies compared to the Gulf Stream region (Fig. 4a). Notice that N^2 in the mixed layer approaches zero (dashed lines in Figs. 4d–f) and becomes problematic for the inversion. We therefore apply the mixed-layer-averaged N^2 as a new surface value and use the linear interpolation between the base of the mixed layer and this surface value to represent the mixed layer stratification (solid lines in Figs. 4d–f).

a. Gulf Stream extension

The total SSD and SSH fields show similar patterns, with warmer and lighter water to the south, with larger values of SSH (Fig. 3a). The correlation between SSH and SSD anomalies (i.e., SSH and SSD after subtraction of the low-pass filtered fields $\langle\cdot\rangle$) varies spatially (Fig. 4a). It is poor around 41°N where two big eddies are evident in SSH, but not in SSD anomaly. Such a lack of consistency in spatial correlation is similar to what is observed in satellite data (e.g., Fig. 1).

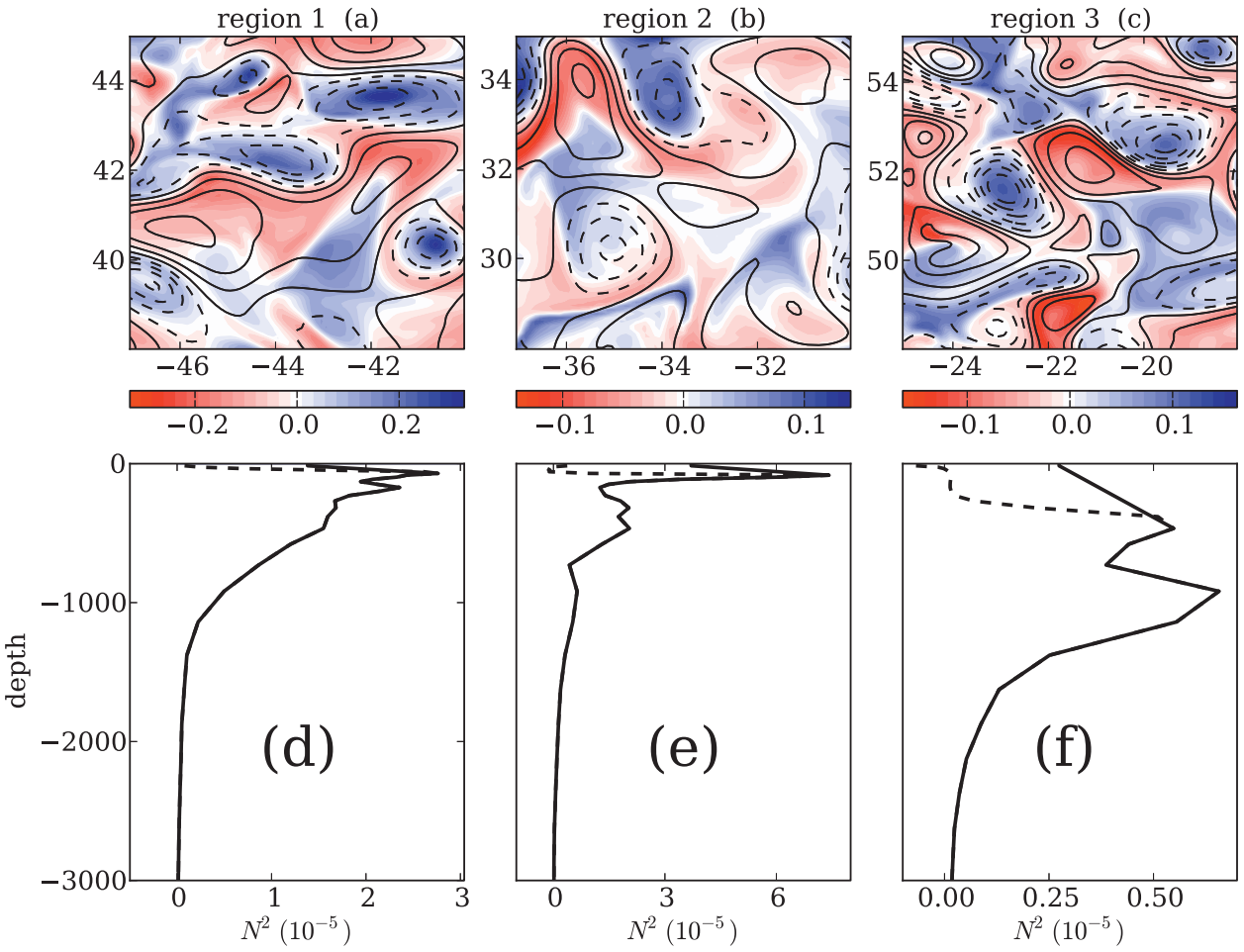

FIG. 4. (a)–(c) Anomaly in the SSD (color) and SSH (contours) calculated by subtraction of the corresponding low-pass-filtered surface fields from the model for the period 23–29 Jan 1995. (d)–(f) Area-averaged stratification N^2 from the PE model (dashed lines) for the same time. Solid lines are the N^2 used in the diagnosis of the isQG solution (note that the x axis differs among subplots) constructed as a linear interpolation between the mixed layer average N^2 imposed at the surface, and the value at the mixed layer base. Region 1 is shown in (a),(d), region 2 in (b),(e), and region 3 in (c),(f).

We calculated the SQG solution $\psi^s(x, y, z)$ from the SSD field (Fig. 4a) and the area-averaged $N^2(z)$ (Fig. 4d) using the numerical method described in the appendix. The SQG solution decays with depth (gray line in Fig. 5a). The difference between the surface pressure (SSH) and SQG estimate is the residual, which is accounted by the interior solution $\psi^i(x, y, 0)$, comprised of the barotropic and first baroclinic modes $F_{0,1}$ (Fig. 5; see appendix for details). The modal amplitudes are determined by the constraint that the two modes sum to give the residual pressure at the surface and cancel each other at the bottom boundary. The first baroclinic mode is surface intensified, as is typical of the ocean (e.g., Kundu and Allen 1975).

The vertical derivative of the modes reflects the vertical structure of the density anomaly associated with the eddy field. It is zero at the surface and bottom for the baroclinic modes $F_{1,2}$ by definition (the solid and dashed lines in Fig. 5b), and nonzero for the SQG solution (the gray line in Fig. 5b). The subsurface maximum occurs around $z = -500$ m for the first baroclinic mode (the solid line in Fig. 5b), and just below the mixed layer in the SQG solution (the gray line in Fig. 5b). The barotropic mode does not contribute to the density structure.

The vertical structure of the rms perturbation kinetic energy $0.5(\psi_y^2 + \psi_x^2)$ and density $\psi_z(\rho_0 f_0)g^{-1}$ for each solution, ψ^s and ψ^i, is compared with that of the PE model shown in Fig. 6. The surface solution (gray line Fig. 6a) yields a small but significant contribution to the total EKE in the upper 500 m, while the interior solution has a larger contribution (dashed line Fig. 6a). When combined, the total reconstructed EKE (solid line Fig. 6a) agrees well with the PE model solution (symbols in Fig. 6a), especially in the upper 500 m.

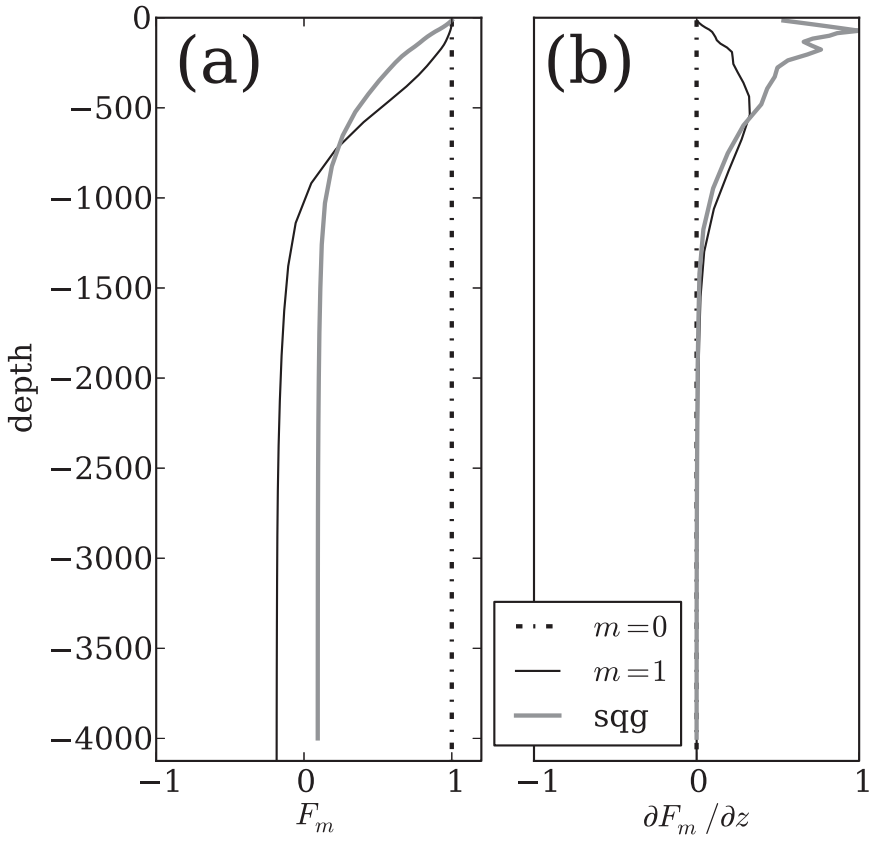

FIG. 5. (a) First three eigenmodes $F_{0,1,2}(z)$ and the SQG solution $\psi^s(z)$ (gray line) normalized by their maximum values. They are calculated based on the N^2 profile shown in Fig. 4d. (b) Vertical derivative of $F_{0,1,2}(z)$, which is related to the density anomaly. There is no density anomaly associated with the barotropic mode (F_0). Only the first two modes $F_{0,1}$ are used in constructing the interior solution.

Note that the total EKE is differs from the sum of the EKE derived from ψ^i and ψ^s separately; specifically

$$\frac{1}{2}|\mathbf{v}^t|^2 = \frac{1}{2}|\mathbf{v}^i|^2 + \frac{1}{2}|\mathbf{v}^s|^2 + \mathbf{v}^s \cdot \mathbf{v}^i. \tag{26}$$

We will denote the four terms from left to right as EKE^t, EKE^i, EKE^s, and $\mathrm{EKE}^{i\cdot s}$. The cross-correlation term, $\mathrm{EKE}^{i\cdot s}$, is generally nonzero. For example, in the case shown in Fig. 6, EKE^i, EKE^s, and $\mathrm{EKE}^{i\cdot s}$ account for 60%, 20%, and 20% of EKE^t, respectively. Furthermore, $\mathrm{EKE}^{i\cdot s}$ can be negative, so that both EKE^i and EKE^s may in themselves be larger than EKE^t, as in the case of the high-latitude region described below.

The rms density of the interior solution (dashed line in Fig. 6d) is zero at the surface by definition so that it entirely fails at reconstructing the density anomaly in the PE model (symbols in Fig. 6d). However, combined with the SQG solution, which has maximum density variations in upper layers (gray line in Fig. 6d), the total reconstructed density field (solid line in Fig. 6d) matches the PE model quite well.

Plan views of the density at 290-m depth show that the SQG solution resembles the observed density anomaly in some regions but not in others (Fig. 7a). It generally also has smaller amplitude. The interior solution ρ^i more closely resembles the actual field (Fig. 7b), and the sum of the two (Fig. 7c) is nearly identical to the PE model density (Fig. 7d), both in terms of structure and amplitude.

The density anomaly associated with the surface solution is surface trapped, which is clearly shown in a vertical cross section of the density field (Fig. 8a), while the interior solution has a maximum at around 500-m depth (Fig. 8b). Neither of the two fields alone captures the PE model solution (Fig. 8d), but their combination (Fig. 8c) yields a good estimate. At 42°W (Fig. 8), only a combination of surface and interior solutions can represent the change in sign of density anomaly with depth. Without the SQG solution, higher baroclinic

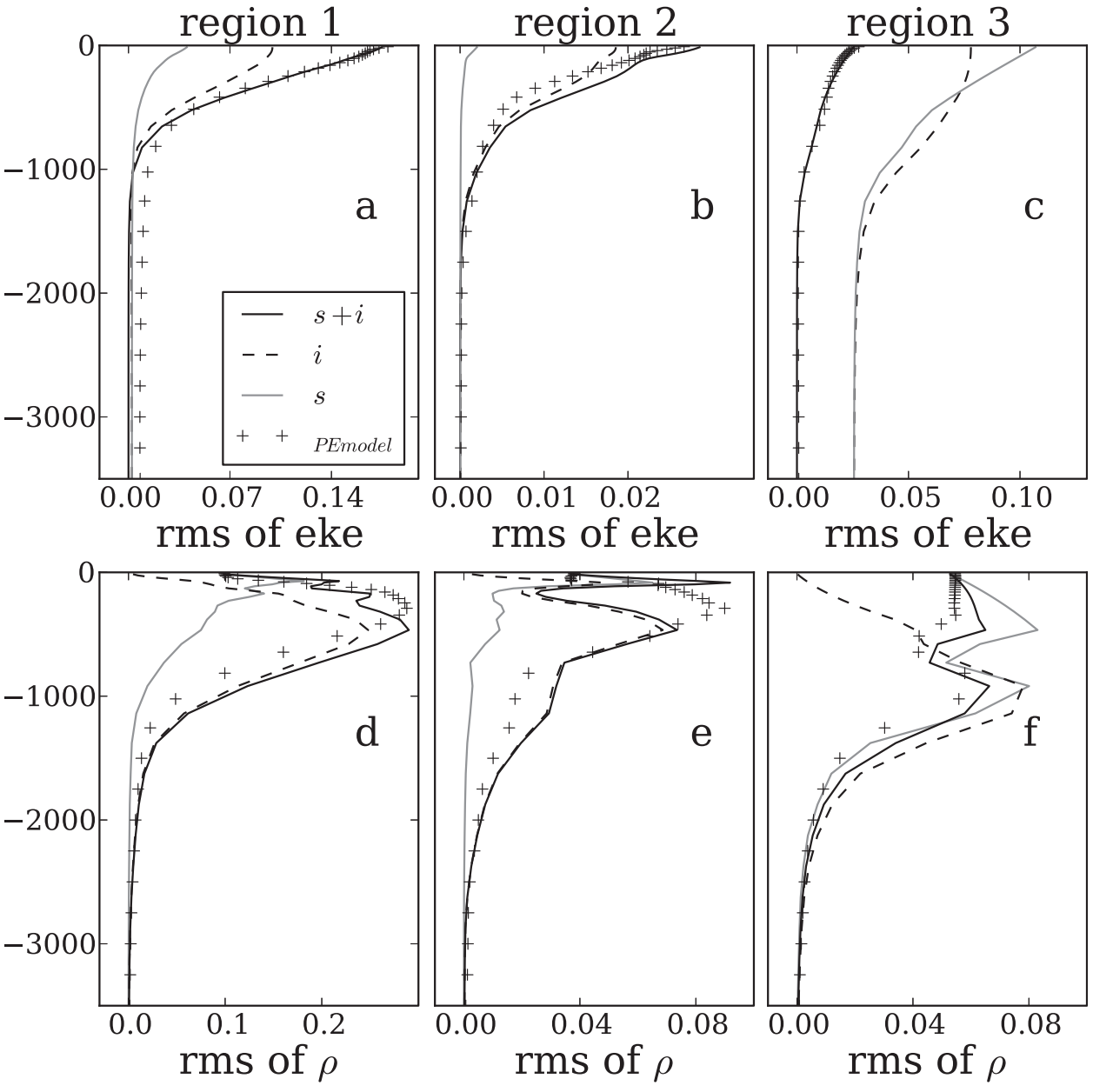

FIG. 6. The rms of (a)–(c) the perturbation kinetic energy and (d)–(f) density ρ derived from surface ψ^s (gray), interior ψ^i (dashed), total isQG solution $\psi^s + \psi^i$ (solid black), and the true value in the PE model (symbols) for (a),(d) region 1, (b),(e) region 2, and (c),(f) region 3.

modes need to be included to capture this shallow dipole structure. But using the SQG solution to represent the upper layer reduces the number of interior baroclinic modes required for a good reconstruction.

A somewhat more sensitive test comes with comparing the subsurface relative vorticity, as this highlights smaller scales in the flow field (Figs. 7e,f). In general, the diagnosed vorticity $\zeta^t = \nabla^2(\psi^t) = \nabla^2(\psi^i + \psi^s)$ (Fig. 7e) is quite similar to the PE vorticity field (Fig. 7f), both in structure and amplitude. The PE vorticity exhibits finer structure and is larger in magnitude at some locations, but ζ^t represents the horizontal distribution and vertical structure (not shown) quite well, especially above 1000-m depth. Similar results were obtained in several other subdomains around the Gulf Stream where lateral density gradients are strong.

b. *Eastern subtropical gyre*

In this region, the SSD and SSH anomaly fields are mostly uncorrelated (Fig. 4b), suggesting the SQG solution

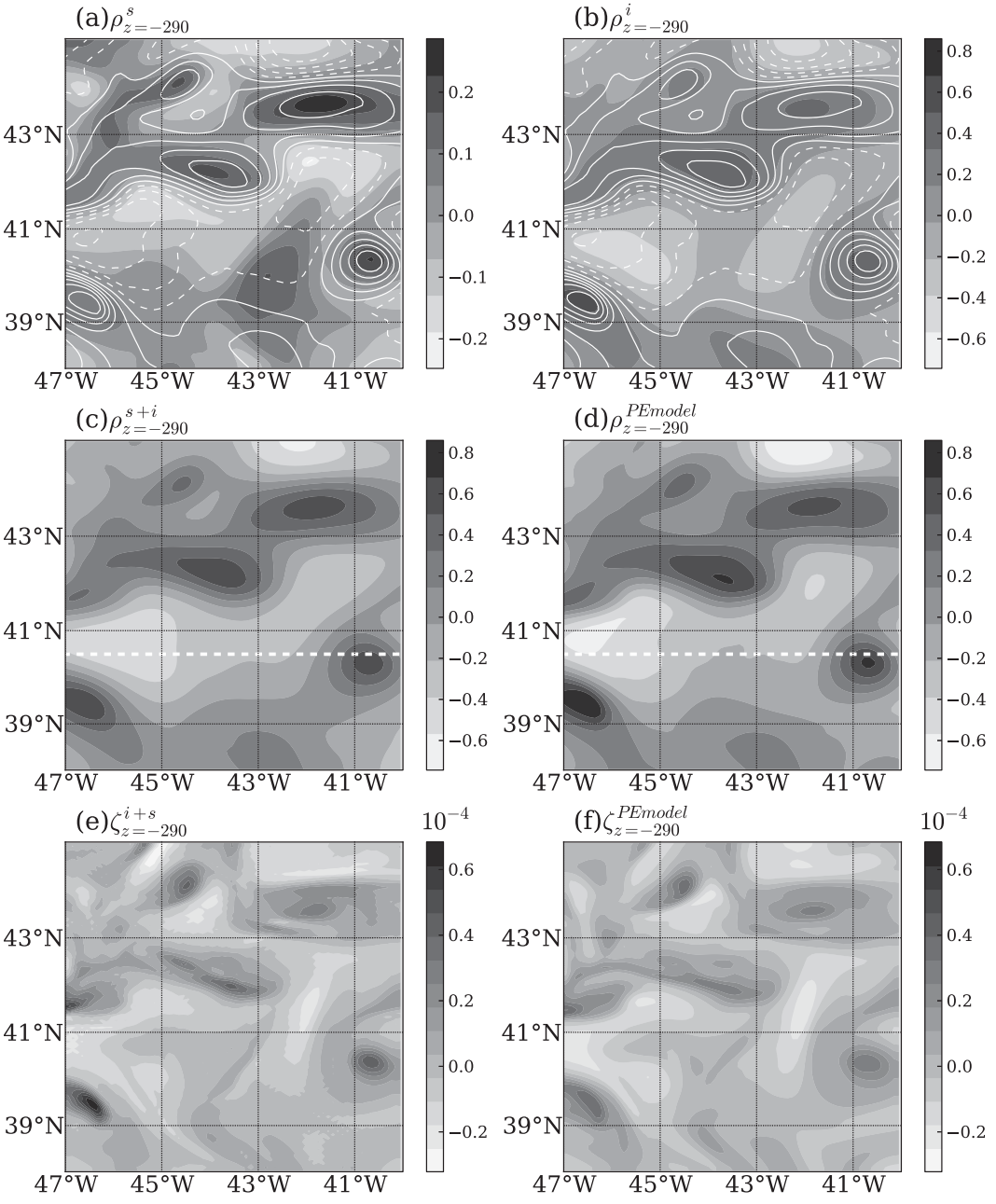

FIG. 7. (a)–(d) The density at 290 m for region 1; (a) ρ^s, (b) ρ^i, (c) $\rho^s + \rho^i$, and (d) the PE model density. The PE model density in (d) is plotted with white contours in (a),(b) for comparison. The vertical component of the relative vorticity (s^{-1}) at 290 m for (e) the total reconstructed field and (f) the PE model are shown. Dashed lines in (c),(d) show the location of the vertical section shown in Fig. 8.

by itself would be inadequate. This region is distinguished by a large value of N^2, whose profile shows two subsurface maxima (Fig. 4e), one at the base of the mixed layer, with $N^2 \approx 7.5 \times 10^{-5}\,s^{-2}$, and a second near the thermocline at approximately 400 m.

The SQG solution is much weaker than the interior solution, which has a similar level of energy as the PE model (Fig. 6b). However, the EKE from the combined isQG fields is larger than the sum of the interior and surface EKE because the correlation between ψ^i and ψ^s is positive, leading to large positive $EKE^{i,s}$ in (26).

The predicted density anomaly exhibits two maxima, one near the base of the mixed layer and a second at around 500-m depth, while the PE solution has a single

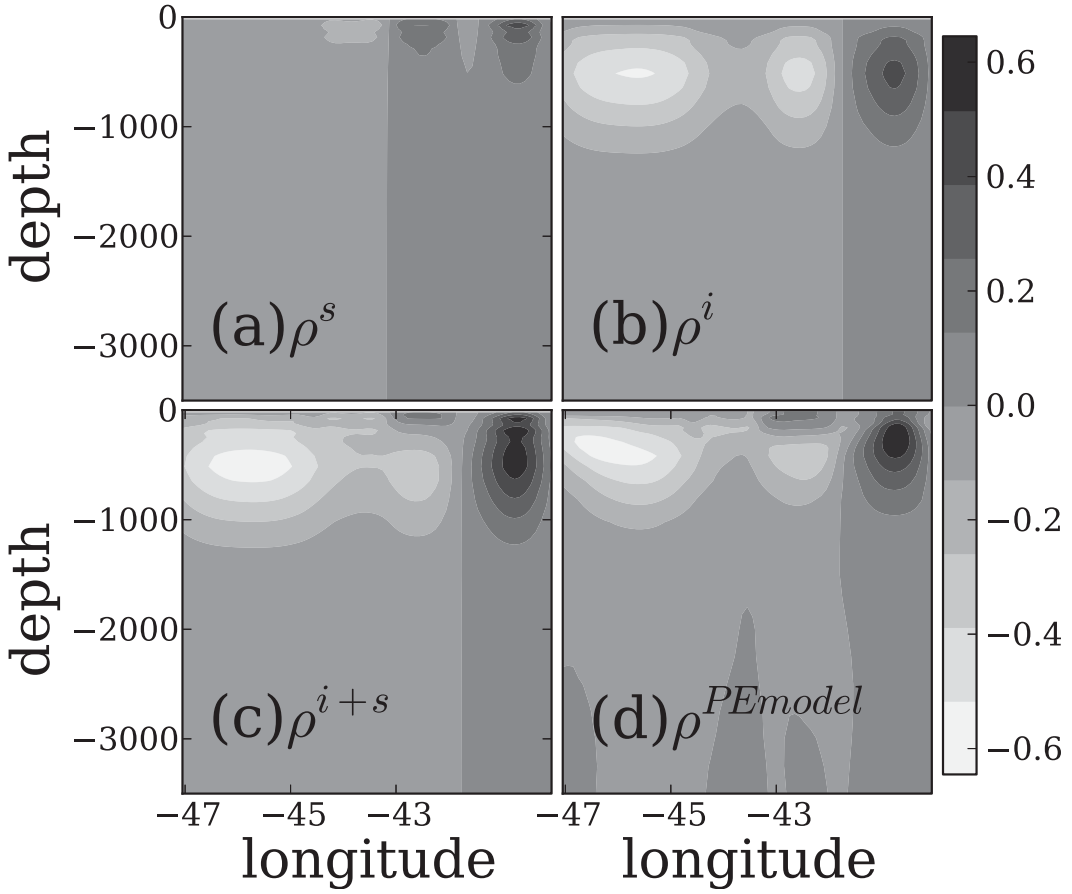

FIG. 8. Vertical sections at 40.4°N in region 1 showing the density anomaly as diagnosed from (a) ρ^s, (b) ρ^i, (c) $\rho^s + \rho^i$, alongside (d) the PE model solution.

subsurface maximum at around 300 m (Fig. 6e). The SQG solution yields the largest rms density anomaly in the upper 100 m while the interior solution dominates below. Though the magnitude is correct, the vertical structure is not. This is because as the surface contribution is suppressed by the strong stratification, the two gravest modes, F_0 and F_1, are not enough to reconstruct the fine structure of the upper ocean.

The diagnosed density anomaly nevertheless agrees fairly well with the PE model as viewed in the horizontal plane (Figs. 9a,b). With few exceptions (e.g., at 34°N, 31°W), the eddies are well captured by $\rho^s + \rho^i$, especially in structure. The reconstructed field is weaker than the PE model at 290 m, as also inferred from the rms density profile in Fig. 6e. The reconstructed density field at 500 m (not shown) is a much better representation of the PE model result both in structure and magnitude. In summary, the reconstructed fields correctly predict the density anomalies, but misrepresent the vertical structure for Region 2.

The predicted vorticity at 290 m is also reasonably accurate (Figs. 9c,d). While some of the filaments are misrepresented, the eddies are by and large correct, both in structure and location. As the vertical variation of EKE is better represented than density, the predicted vorticity is better than density at other depths, e.g., at 200 m.

Thus the method is reasonably successful also in the Eastern subtropical region, where eddies are weak. The shallow mixed layer here causes a decoupling of the SSD (and hence the SQG solution) from the interior, and as such, the correlation between SSD and SSH is weak, and SSH signal mainly reflects interior dynamics. It is left to the interior solution to capture the density field below the mixed layer. As the interior solution is comprised solely of the barotropic and first baroclinic modes, it fails to fully capture density variations in the upper 400 m. Including higher baroclinic modes could plausibly remedy this.

c. *High latitude*

The SSD and SSH fields over the high-latitude region are fairly well correlated over much of the domain, with

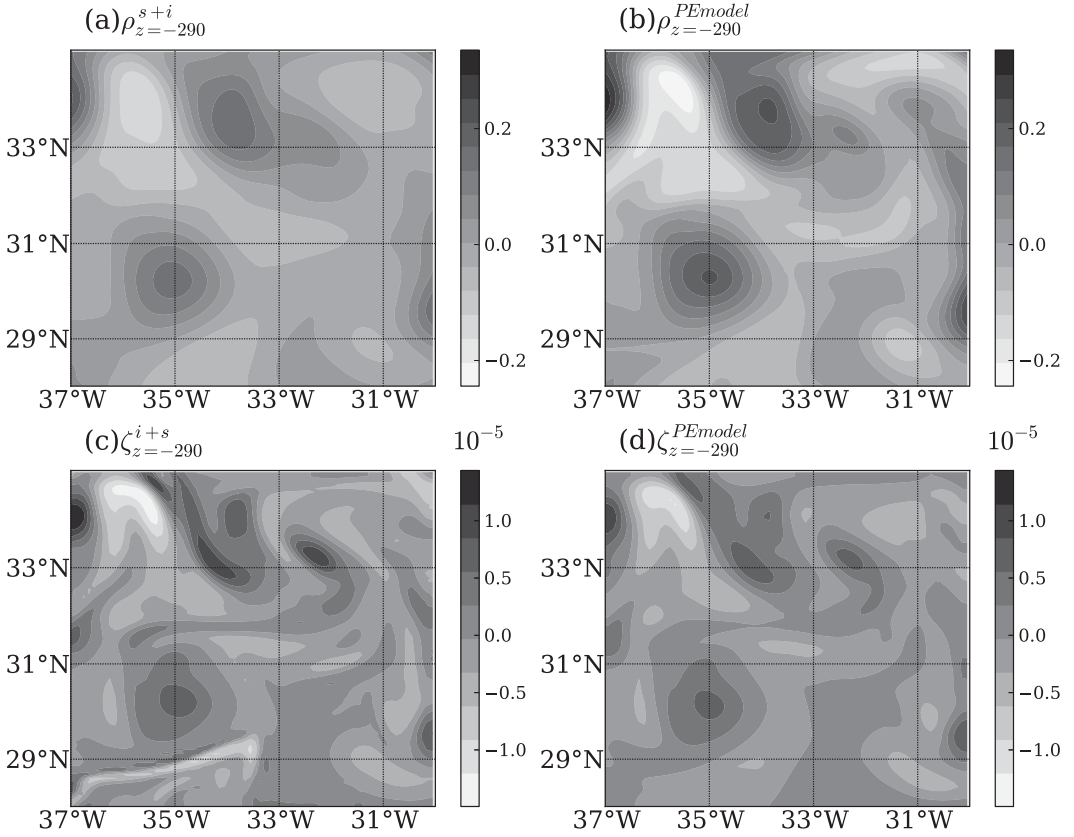

FIG. 9. (a) The diagnosed isQG density anomaly, (b) the PE model density anomaly, (c) the isQG relative vorticity (s^{-1}), and (d) the PE model relative vorticity at 290 m in region 2.

some exceptions as well (Fig. 4c). As in the eastern region, the stratification exhibits two subsurface maxima, at the base of the mixed layer (330 m) and near the thermocline at 1000 m (Fig. 4f). The stratification is otherwise weak, with a maximum N^2 less than $7 \times 10^{-6}\,s^{-2}$.

In the reconstructed field, there is a strong cancellation between the surface and interior solutions. Both the eddy kinetic energy in the interior EKE^i and the surface EKE^s exceed the total eddy kinetic energy EKE^t. This is because $EKE^{i,s}$ is negative, implying a strong cancellation between the interior and surface solutions. The surface solution decays slowly with depth especially for eddies larger than the deformation radius, so that the interior solution must balance it to satisfy the no-velocity condition at the ocean bottom. The combined solution correctly captures the vertical scale and magnitude of the variances. The predicted density even captures the minimum rms density at 700 m seen in the PE model (Fig. 6f).

The density and vorticity fields are well captured at 290 m (Fig. 10) both in structure and amplitude. Even the filamentary structures are captured by the reconstruction.

The vertical cross sections of density and vorticity (not shown) support the notion that the interior solution compensates the surface solution to limit the vertical penetration. Neither component fully captures the observed field by itself—a combination is required. The fact that the PE model fields (as well as observed velocities) decay at depth supports the imposition of the zero velocity condition at the bottom.

4. Summary and discussion

A method for reconstructing interior velocity and density fields from sea surface density and height is proposed and evaluated using output from a high-resolution numerical simulation. The method employs the QG approximation and combines the interior plus surface (isQG) decompositions. In particular, the sea surface density is not assumed to be correlated with surface height. Rather, the surface height reflects in part the influence of the interior PV, which is assumed to be zero in most SQG reconstructions.

We use surface density to infer the SQG portion of the solution and then use the residual SSH anomaly to

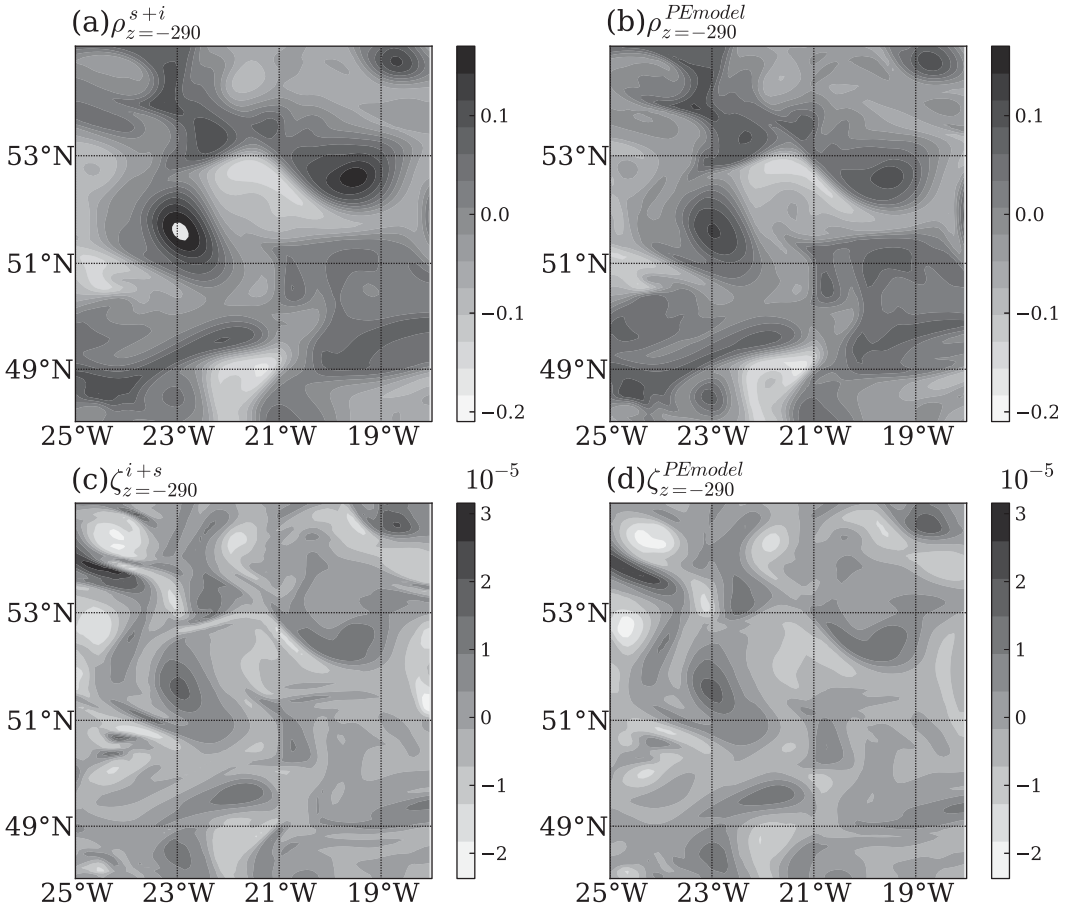

FIG. 10. As in Fig. 9, but for region 3.

determine the interior PV and its associated interior flow. However, the method is quasigeostrophic, and finer-scale features that are out of QG balance, such as submesoscale fronts and filaments, may not be resolved. An important feature of the solution method presented here is that it reconstructs the eddy field, or anomaly from background state, using the anomaly in sea surface density and SSH. To compare the results with measurements, it may become necessary to estimate the background flow using a similar approach to what is described here.

The method is evaluated for three 7° × 7° regions in a model of the North Atlantic, each of which are characterized by different dynamics. The method successfully predicts the subsurface velocity and density fields in all three regions, down to roughly 1000-m depth. Nevertheless, it does not fully capture the vertical variation of density in the eastern subtropical Atlantic. But in all cases, the lateral structure and, generally, the amplitude of the mesoscale eddies is captured.

The results shown are for the boreal winter, but we also tested the method in the summer months when surface stratification is stronger. The SQG solution is found to decay more rapidly with depth in summer as compared to winter, much like the eastern subtropical gyre region (e.g., Fig. 6e) and thus hardly contributes to the surface height (pressure) field. When the density of the surface layer is significantly influenced by atmospheric forcing it becomes decoupled from the interior dynamics, as in Isern-Fontanet et al. (2008). The interior reconstruction is then dominated by the barotropic and first baroclinic modes.

The development of the isQG approach is largely motivated by wanting to reconstruct the subsurface velocity and density fields in the ocean using satellite data. Here, we demonstrate its applicability by using a regional PE model simulation, but there are several potential difficulties with using satellite data. Most importantly, the method requires surface density, and by using SST as a proxy for density, the method may be practicable only in regions where temperature dominates the density variations. For regions where SST and SSS compensate, using SST alone in the density calculation will yield an overestimation of density gradients (Rudnick and Ferrari 1999; Isern-Fontanet et al. 2008).

However, we expect that in the future, salinity data from satellite missions like Aquarius and SMOS may be used to overcome this constraint by including salinity in the estimate of surface density. The current satellite SST products have high spatial and temporal resolution [e.g., 9-km products at near-daily frequency from the Group for High Resolution Sea Surface Temperature (GHRSST) project], but most gridded SSH data have low temporal resolution (~10 days) and spatial resolution of about 25 km on average, which marginally resolves mesoscale eddies in midlatitudes. The combined product from multiple altimeters could also lack accuracy in the position of eddies (Pascual et al. 2006). In the future, this difficulty may be alleviated by the Surface Water and Ocean Topography (SWOT) mission that will provide SSH at much higher resolutions.

In addition to the surface fields, the method requires the vertical profile of stratification $N^2(z)$. We find the reconstruction is not sensitive to slight changes in N^2 as long as the surface value is not infinitesimal. We expect the N^2 diagnosed from monthly mean climatology, constructed using Argo data for example, will produce an adequate representation of the average $N^2(z)$ within a region for a particular month. A strategy for representing the mixed layer is to use an estimate of the mixed layer depth Δh based on the density increment of $\Delta\rho$ from the surface (often taken to be 0.05), and calculate the surface stratification using $N^2 = -(g/\rho)\Delta\rho/\Delta h$. This can then be linearly interpolated to N^2 at the base of the mixed layer. In regions where the horizontal variation of the stratification is large, the area-averaged N^2 profile may not be sufficient for reconstructing the subsurface flow field. One may then consider using a local $N^2(x, y, z)$ in calculating the vertical eigenmodes and SQG solution.

At present, only two eigenmodes are used to represent the interior solution. In addition to prescribing a surface pressure boundary condition, we assume the lower boundary has no velocity for calculating the amplitude of each of the two modes. But, if one has more information about the interior, from a mooring, for example, one could include more eigenmodes or provide a more accurate lower boundary condition.

Based on comparison with PE model fields, the proposed isQG method shows great potential for extending current SSH-based estimates of the surface geostrophic velocity field to depth (upper 1000 m of the ocean). The method may be extended for diagnosing vertical velocities, although higher-order Rossby number dynamics may need to be considered. Such reconstructed fields have applicability for initialization of models and data assimilation into models. A successful reconstruction of the subsurface flow field from satellite data can tremendously expand our knowledge of the ocean. However, more quantitative analyses are needed for evaluating this method against observations before such reconstructed fields can be used in scientific applications.

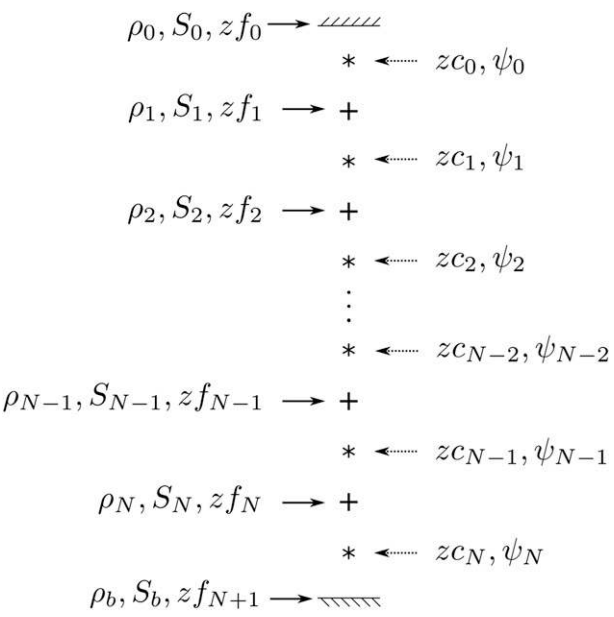

FIG. A1. Variable arrangement in a stagger vertical grid, where $S_i = f^2/N^2$ at zf_i.

Acknowledgments. We thank Shafer Smith for helpful comments. JW and AM were supported by NASA (NNX12AD47G) and NSF (OCE 0928617). JLM was supported by the Office of Naval Research and the Office of Science (BER), U.S. Department of Energy under DE-GF0205ER64119. Computer time for the GCM simulation was provided through the Department of Defense High Performance Computing Modernization Office at the Naval Oceanographic Office (NAVO) in Mississippi. GRF is supported by OCE-0752346 and JHL by NORSEE (Nordic Seas Eddy Exchanges) funded by the Norwegian Research Council.

APPENDIX

Numerical Solution

a. Solving the SQG equation

The QG equation to be solved is

$$\begin{aligned} &\mathcal{L}\psi = Q, \\ &\psi_z = b^s/f \quad \text{at} \quad z = 0, \\ &\psi_z = b^b/f \quad \text{at} \quad z = -H, \quad \text{and} \\ &\mathcal{L} \equiv \left(\frac{\partial}{\partial z}\frac{f^2}{N^2}\frac{\partial}{\partial z} + \nabla^2\right), \end{aligned} \tag{A1}$$

where b^s and b^b represent the buoyancy $b = -g\rho'/\rho_0$ at the ocean surface and bottom, f is the Coriolis parameter, N^2 is buoyancy, and Q is the QG potential vorticity. The equation in Fourier space is

$$\left(\frac{\partial}{\partial z}\frac{f^2}{N^2}\frac{\partial}{\partial z} - K^2\right)\hat{\psi} = \hat{Q}; \quad K^2 = k^2 + l^2,$$
$$\hat{\psi}_z = \hat{b}^s/f \quad \text{at} \quad z = 0, \quad \text{and}$$
$$\hat{\psi}_z = \hat{b}^b/f \quad \text{at} \quad z = -H, \tag{A2}$$

which is an ordinary differential equation with two Neumann boundary conditions. We numerically solve this ODE using the finite-difference method. The equation is discretized on a staggered grid. The arrangement of variables is shown in Fig. A1. In this study, we look for SQG solution assuming the bottom buoyancy anomaly and interior PV is zero: $b_b = 0$ and $Q = 0$.

Assuming the grids are equally spaced, the discretized form of the right-hand side of (A2) is $(\mathbf{M}_1 - \mathbf{M}_2)\mathbf{P}_{k,l}$, where

$$\mathbf{M}_1 = \frac{1}{dz^2}\begin{Bmatrix} dz & -dz & 0 & 0 & \cdots & 0 & 0 & 0 & 0 \\ S_1 & -S_1 - S_2 & S_2 & 0 & \cdots & 0 & 0 & 0 & 0 \\ 0 & S_2 & -S_2 - S_3 & S_3 & \cdots & 0 & 0 & 0 & 0 \\ \vdots & \vdots & \vdots & \vdots & \ddots & \vdots & \vdots & \vdots & \vdots \\ 0 & 0 & 0 & 0 & \cdots & S_{N-2} & -S_{N-2} - S_N & S_{N-1} & 0 \\ 0 & 0 & 0 & 0 & \cdots & 0 & S_{N-1} & -S_{N-1} - S_N & S_N \\ 0 & 0 & 0 & 0 & \cdots & 0 & 0 & dz & -dz \end{Bmatrix}$$

in which S_i represents f^2/N^2 at $z = zf_i$,

$$\mathbf{M}_2 = K^2\begin{Bmatrix} 0 & 0 & 0 & 0 & \cdots & 0 & 0 & 0 & 0 \\ 0 & 1 & 0 & 0 & \cdots & 0 & 0 & 0 & 0 \\ 0 & 0 & 1 & 0 & \cdots & 0 & 0 & 0 & 0 \\ \vdots & \vdots & \vdots & \vdots & \ddots & \vdots & \vdots & \vdots & \vdots \\ 0 & 0 & 0 & 0 & \cdots & 0 & 1 & 0 & 0 \\ 0 & 0 & 0 & 0 & \cdots & 0 & 0 & 1 & 0 \\ 0 & 0 & 0 & 0 & \cdots & 0 & 0 & 0 & 0 \end{Bmatrix}$$

and

$$\mathbf{P}_{k,l} = (\hat{\psi}_0, \hat{\psi}_1, \cdots, \hat{\psi}_{N-1}, \hat{\psi}_N)^{\mathrm{T}},$$

where the superscript T represents vector transpose.

The boundary value problem (A2) is discretized into a linear system:

$$(\mathbf{M}_1 - \mathbf{M}_2)\mathbf{P}_{k,l} = \mathbf{R}_{k,l},$$

where

$$\mathbf{R}_{k,l} = \frac{\widehat{b^s}(k,l)}{f}(1, 0, 0 \cdots 0, 0, 0)^{\mathrm{T}}.$$

Then $\mathbf{P}_{k,l} = (\mathbf{M}_1 - \mathbf{M}_2)^{-1}\mathbf{R}_{k,l}$. The dimensions of $\mathbf{M}_{1,2}$ and $\mathbf{R}$ are $(N + 1, N + 1)$ and $(N + 1, 1)$, respectively.

The streamfunction of the SQG solution in physical space can be calculated by

$$\psi^s(x, y, z) = \mathcal{F}^{-1}[\mathbf{P}(k, l, z)], \tag{A3}$$

where $\mathcal{F}^{-1}$ represents an inverse Fourier transform in (k, l) space.

b. Vertical eigenmode decomposition

The interior barotropic and baroclinic modes F_m are eigensolutions of

$$\frac{\partial}{\partial z}\frac{f^2}{N^2}\frac{\partial}{\partial z}F_m = -\frac{1}{R_m^2}F_m. \tag{A4}$$

The discretetized form of this Sturm–Liouville operator $(\partial/\partial z)(f^2/N^2)(\partial/\partial z)$ is

$$\mathbf{M} = \frac{1}{dz^2}\begin{Bmatrix} -S_1 & S_1 & 0 & 0 & \cdots & 0 & 0 & 0 & 0 \\ S_1 & -S_1 - S_2 & S_2 & 0 & \cdots & 0 & 0 & 0 & 0 \\ 0 & S_2 & -S_2 - S_3 & S_3 & \cdots & 0 & 0 & 0 & 0 \\ \vdots & \vdots & \vdots & \vdots & \ddots & \vdots & \vdots & \vdots & \vdots \\ 0 & 0 & 0 & 0 & \cdots & S_{N-2} & -S_{N-2} - S_N & S_{N-1} & 0 \\ 0 & 0 & 0 & 0 & \cdots & 0 & S_{N-1} & -S_{N-1} - S_N & S_N \\ 0 & 0 & 0 & 0 & \cdots & 0 & 0 & S_b & -S_b \end{Bmatrix}.$$

Then F_m and R_m^{-1} are the eigenfunctions and eigenvalues of the matrix **M**.

Note that **M** and $\mathbf{M}_1$ differ in the first and last rows, which represent two different boundary conditions. The difference matrix for varying grid size should be straightforward following the above examples.

REFERENCES

Blumen, W., 1978: Uniform potential vorticity flow. Part I: Theory of wave interactions and two-dimensional turbulence. *J. Atmos. Sci.,* **35,** 774–783.

Bretherton, F. P., 1966: Critical layer instability in baroclinic flows. *Quart. J. Roy. Meteor. Soc.,* **92,** 325–334.

Charney, J. G., 1971: Geostrophic turbulence. *J. Atmos. Sci.,* **28,** 1087–1095.

——, and G. R. Flierl, 1981: Oceanic analogues of large-scale atmospheric motions. *Evolution of Physical Oceanography,* B. Warren and C. Wunsch, Eds., MIT Press, 504–548.

Chelton, D. B., M. G. Schlax, and R. M. Samelson, 2011: Global observations of nonlinear mesoscale eddies. *Prog. Oceanogr.,* **91,** 167–216, doi:10.1016/j.pocean.2011.01.002.

Doney, S. C., S. Yeager, G. Danabasoglu, W. G. Large, and J. C. Mcwilliams, 2003: Modeling global oceanic inter-annual variability (1958-1997): Simulation design and model-data evaluation. NCAR Tech. Note NCAR/TN-452+STR, 48 pp.

Eady, E. T., 1949: Long waves and cyclone waves. *Tellus,* **1,** 33–52.

Ferrari, R., and C. Wunsch, 2010: The distribution of eddy kinetic and potential energies in the global ocean. *Tellus,* **62A,** 92–108.

Fu, L. L., and G. R. Flierl, 1980: Nonlinear energy and enstrophy transfers in a realistically stratified ocean. *Dyn. Atmos. Oceans,* **4,** 219–246.

Hoskins, B. J., 1975: The geostrophic momentum approximation and the semigeostrophic equations. *J. Atmos. Sci.,* **32,** 233–242.

——, M. E. McIntyre, and A. W. Robertson, 1985: On the use and significance of isentropic potential vorticity maps. *Quart. J. Roy. Meteor. Soc.,* **111,** 877–946.

Isern-Fontanet, J., B. Chapron, G. Lapeyre, and P. Klein, 2006: Potential use of microwave sea surface temperatures for the estimation of ocean currents. *Geophys. Res. Lett.,* **33,** L24608, doi:10.1029/2006GL027801.

——, G. Lapeyre, P. Klein, B. Chapron, and M. W. Hecht, 2008: Three-dimensional reconstruction of oceanic mesoscale currents from surface information. *J. Geophys. Res.,* **113,** C09005, doi:10.1029/2007JC004692.

Klein, P., J. Isern-Fontanet, G. Lapeyre, G. Roullet, E. Danioux, B. Chapron, S. Le Gentil, and H. Sasaki, 2009: Diagnosis of vertical velocities in the upper ocean from high-resolution sea surface height. *Geophys. Res. Lett.,* **36,** L12603, doi:10.1029/2009GL038359.

Kundu, P., and J. S. Allen, 1975: Modal decomposition of the velocity field near the Oregon coast. *J. Phys. Oceanogr.,* **5,** 683–705.

LaCasce, J. H., 2012: Surface quasigeostrophic solutions and baroclinic modes with exponential stratification. *J. Phys. Oceanogr.,* **42,** 569–580.

——, and A. Mahadevan, 2006: Estimating subsurface horizontal and vertical velocities from sea-surface temperature. *J. Mar. Res.,* **64,** 695–721.

Lapeyre, G., 2009: What vertical mode does the altimeter reflect? On the decomposition in baroclinic modes and on a surface-trapped mode. *J. Phys. Oceanogr.,* **39,** 2857–2874.

——, and P. Klein, 2006: Dynamics of the upper oceanic layers in terms of surface quasigeostrophy theory. *J. Phys. Oceanogr.,* **36,** 165–176.

Large, W. G., J. C. Mcwilliams, and S. C. Doney, 1994: Oceanic vertical mixing: A review and a model with a nonlocal boundary layer parameterization. *Rev. Geophys.,* **32,** 363–403.

McClean, J. L., P.-M. Poulain, J. W. Pelton, and M. E. Maltrud, 2002: Eulerian and lagrangian dtatistics from surface drifters and a high-resolution POP simulation in the north Atlantic. *J. Phys. Oceanogr.,* **32,** 2472–2491.

Pascual, A., Y. Faugère, G. Larnicol, and P.-Y. Le Traon, 2006: Improved description of the ocean mesoscale variability by combining four satellite altimeters. *Geophys. Res. Lett.,* **33,** L02611, doi:10.1029/2005GL024633.

Pedlosky, J., 1987: *Geophysical Fluid Dynamics*. 2nd ed. Springer-Verlag, 710 pp.

Phillips, N. A., 1954: Energy transformations and meridional circulations associated with simple baroclinic waves in a two-level, quasi-geostrophic model. *Tellus,* **6,** 273–286.

Reynolds, R. W., T. M. Smith, C. Liu, D. B. Chelton, K. S. Casey, and M. G. Schlax, 2007: Daily high-resolution-blended analyses for sea surface temperature. *J. Climate,* **20,** 5473–5496.

Rossow, W. B., and R. A. Schiffer, 1991: ISCCP cloud data products. *Bull. Amer. Meteor. Soc.,* **72,** 2–20.

Rudnick, D., and R. Ferrari, 1999: Compensation of horizontal temperature and salinity gradients in the ocean mixed layer. *Science (New York, N.Y.),* **283,** 526–529.

Scott, R. B., and D. G. Furnival, 2012: Assessment of traditional and new eigenfunction bases applied to extrapolation of surface geostrophic current time series to below the surface in an idealized primitive equation simulation. *J. Phys. Oceanogr.,* **42,** 165–178.

Smith, K. S., and G. K. Vallis, 2001: The scales and equilibration of midocean eddies: Freely evolving flow. *J. Phys. Oceanogr.,* **31,** 554–571.

——, and J. Vanneste, 2013: A surface-aware projection basis for quasigeostrophic flow. *J. Phys. Oceanogr.,* **43,** 548–562.

Smith, R. D., M. E. Maltrud, F. O. Bryan, and M. W. Hecht, 2000: Numerical simulation of the North Atlantic Ocean at 1/10°. *J. Phys. Oceanogr.,* **30,** 1532–1561.

Spencer, R. W., 1993: Global oceanic precipitation from the MSU during 1979–91 and comparisons to other climatologies. *J. Climate,* **6,** 1301–1326.

Stammer, D., 1997: Global characteristics of ocean variability estimated from regional TOPEX/Poseidon altimeter measurements. *J. Phys. Oceanogr.,* **27,** 1743–1769.

Tulloch, R., and K. S. Smith, 2006: A new theory for the atmospheric energy spectrum: Depth-limited temperature anomalies at the tropopause. *Proc. Natl. Acad. Sci. USA,* **103,** 14 690–14 694.

——, and ——, 2009: Quasigeostrophic turbulence with explicit surface dynamics: Application to the atmospheric energy spectrum. *J. Atmos. Sci.,* **66,** 450–467.

Wunsch, C., 1997: The vertical partition of oceanic horizontal kinetic energy. *J. Phys. Oceanogr.,* **27,** 1770–1794.

Xie, P., and P. A. Arkin, 1997: Global precipitation: A 17-year monthly analysis based on gauge observations, satellite estimates, and numerical model outputs. *Bull. Amer. Meteor. Soc.,* **78,** 2539–2558.